sensors

MDPI

Article

Synthesis, Characterization, and Sensor Applications of Spinel $ZnCo_2O_4$ Nanoparticles

Juan Pablo Morán-Lázaro [1,*], Florentino López-Urías [2], Emilio Muñoz-Sandoval [2], Oscar Blanco-Alonso [3], Marciano Sanchez-Tizapa [4], Alejandra Carreon-Alvarez [4], Héctor Guillén-Bonilla [5], María de la Luz Olvera-Amador [6], Alex Guillén-Bonilla [1] and Verónica María Rodríguez-Betancourtt [7]

1 Department of Computer Science and Engineering, CUValles, University of Guadalajara, Ameca, Jalisco 46600, Mexico; alex.guillen@profesores.valles.udg.mx
2 Advanced Materials Department, IPICYT, San Luis Potosí, S.L.P. 78216, Mexico; flo@ipicyt.edu.mx (F.L.-U.); ems@ipicyt.edu.mx (E.M.-S.)
3 Department of Physics, CUCEI, University of Guadalajara, Guadalajara, Jalisco 44410, Mexico; oscar.blanco@cucei.udg.mx
4 Department of Natural and Exact Sciences, CUValles, University of Guadalajara, Ameca, Jalisco 46600, Mexico; msanchez@profesores.valles.udg.mx (M.S.-T.); alejandra.carreon@profesores.valles.udg.mx (A.C.-A.)
5 Department of Project Engineering, CUCEI, University of Guadalajara, Guadalajara, Jalisco 44410, Mexico; hguillenbonilla@gmail.com
6 Department of Electrical Engineering (SEES), CINVESTAV-IPN, Mexico City, DF 07360, Mexico; molvera@cinvestav.mx
7 Department of Chemistry, CUCEI, University of Guadalajara, Guadalajara, Jalisco 44410, Mexico; veronica.rodriguez@red.cucei.udg.mx
* Correspondence: juan.moran@profesores.valles.udg.mx; Tel.: +52-375-7580-500 (ext. 47267)

Academic Editors: Eduard Llobet and Stella Vallejos
Received: 7 October 2016; Accepted: 12 December 2016; Published: 17 December 2016

Abstract: Spinel $ZnCo_2O_4$ nanoparticles were synthesized by means of the microwave-assisted colloidal method. A solution containing ethanol, Co-nitrate, Zn-nitrate, and dodecylamine was stirred for 24 h and evaporated by a microwave oven. The resulting solid material was dried at 200 °C and subsequently calcined at 500 °C for 5 h. The samples were characterized by scanning electron microscopy (SEM), transmission electron microscopy (TEM), X-ray diffraction (XRD), and Raman spectroscopy, confirming the formation of spinel $ZnCo_2O_4$ nanoparticles with average sizes between 49 and 75 nm. It was found that the average particle size decreased when the dodecylamine concentration increased. Pellets containing $ZnCo_2O_4$ nanoparticles were fabricated and tested as sensors in carbon monoxide (CO) and propane (C_3H_8) gases at different concentrations and temperatures. Sensor performance tests revealed an extremely high response to 300 ppm of CO at an operating temperature of 200 °C.

Keywords: spinel; faceted nanoparticle; cobaltite; sensors

1. Introduction

For a long time, pollutant gases from industry and internal combustion engines have been responsible for many human health issues, and to a large extent, for global climate change. Facing this, several groups have focused on the research and development of new sensor materials for the detection and monitoring of polluting gases such as CO and C_3H_8. In particular, sensor materials made from semiconductor oxides have been a valuable choice because they possess good chemical stability,

low price, and an easy integration into electronic circuits. However, it is still necessary to improve sensor parameters such as selectivity, sensitivity, and operating temperature.

Zinc cobaltite ($ZnCo_2O_4$) is a p-type semiconductor material with a spinel-type structure. This material has attracted the attention of several research groups due to its potential applications as an electrode for Li-ion batteries [1–5], as a catalyst [6–9], and in supercapacitors [10–13]. In the gas sensors field, sensor devices based on $ZnCo_2O_4$ nanoparticles have displayed an excellent sensitivity to liquefied petroleum gas [14–17], H_2S [18], ethanol [19,20], acetone [21], and formaldehyde [22,23], probably due to their high surface area. Additionally, $ZnCo_2O_4$ has also been used as Cl_2, NO_2, CO_2, H_2, NH_3, CH_3COOH, SO_2, CO, C_3H_8, ethylene, xylene, toluene, and methanol gas sensors [15,16,18–22]. Specifically, when $ZnCo_2O_4$ nanoparticles were exposed to CO and C_3H_8 concentrations, a poor sensitivity was exhibited at working temperatures in the range of 175 to 350 °C [15,16,19,21]. In contrast, sensors based on nanowire-assembled hierarchical $ZnCo_2O_4$ microstructures showed a good sensitivity towards CO and C_3H_8 at an operating temperature of 300 °C [22]. From these studies, it is fair to assume that the gas sensing properties depend on the shape and size of the nanoparticles [24]. Therefore, developing a $ZnCo_2O_4$-based gas sensor, with a high sensitivity and a low operating temperature, is of great interest to many people. Several synthesis methods of $ZnCo_2O_4$ nanoparticles have been reported, such as combustion [1], hydrothermal [3,12], thermal decomposition [14], co-precipitation/digestion [15], water-in-oil (W/O) microemulsion [18], sol-gel [25], and surfactant-mediated [26] methods. In recent years, the microwave-assisted colloidal method has been an efficient and low-cost synthesis process for obtaining micro and nanostructures of oxide materials [27–29]. In fact, microwave is a simple technique, which plays an important role in colloidal synthesis since it provides a rapid evaporation of the precursor solvent and a short reaction time [30–33].

To the best of our knowledge, there are not reports on the synthesis and use of faceted $ZnCo_2O_4$ nanoparticles for gas sensing applications, such as the ones presented in this investigation, but in recent works, sensors based on faceted SnO_2 and $ZnSn(OH)_6$ nanoparticles exhibited high response towards toluene and ethanol, respectively [34,35]. We believe that materials based on faceted nanoparticles can be strong candidates for gas sensing applications due to their large surface areas.

In this paper, $ZnCo_2O_4$ nanoparticles are synthesized via a microwave-assisted colloidal method [27,36]. The experimental method and the different steps to synthesize $ZnCo_2O_4$ nanoparticles are described in detail. In the following, the results of SEM, XRD, Raman, and TEM characterizations are shown. In addition, sensitivity results for sensors based on $ZnCo_2O_4$ nanoparticles are thoroughly discussed.

2. Materials and Methods

Zinc nitrate hydrate ($Zn(NO_3)_2 \bullet xH_2O$, Sigma Aldrich 99.99%), cobalt(II) nitrate hexahydrate ($Co(NO_3)_2 \bullet 6H_2O$, Sigma Aldrich 98%), dodecylamine ($C_{12}H_{27}N$, Sigma Aldrich 98%), and ethanol (C_2H_6O, Golden Bell 98%) were used as reagents. 5 mmol (0.947 g) of $Zn(NO_3)_2 \bullet xH_2O$, 10 mmol (2.91 g) of ($Co(NO_3)_2 \bullet 6H_2O$, and 5.4 mmol (1 g) of $C_{12}H_{27}N$ were separately dissolved in 5 mL of ethanol. Additional syntheses were made with 10.8 mmol (2 g) and 16.2 mmol (3 g) of dodecylamine in order to obtain additional nanoparticle sizes. After 20 min of vigorous stirring on magnetic dishes at room temperature, the cobalt nitrate solution was added dropwise to the dodecylamine solution and kept stirring for 1 h. The zinc nitrate solution was then slowly added to the cobalt and dodecylamine mixture yielding a wine-color solution (the solutions with 10.8 and 16.2 mmol of dodecylamine were greenish-blue) with pH = 2 and a final volume of approximately 16 mL. This final solution was covered with a watch glass to avoid contamination and kept under stirring for 24 h, losing ~2 mL by evaporation. The solution (~14 mL) was evaporated afterwards using a microwave oven (General Electric JES769WK) at a low power (~140 W). The microwave radiation was applied over the solution for periods of 1 min in order to avoid splashing. The total time of evaporation was 3 h. The resulting solid was dried in air with a muffle (Novatech) at 200 °C. Finally, the calcination of the powder was done at 500 °C for 5 h in

an alumina crucible with a cover at a heating rate of 100 °C/h. The sample was kept in the furnace for cooling at room temperature. The samples made with 5.4, 10.8, and 16.2 mmol of dodecylamine were labeled as A, B, and C, respectively.

The calcined samples were characterized by SEM using a FEI-Helios Nanolab 600 system operated at 20 kV. XRD characterizations were performed with a PANalytical Empyrean system with CuKα and λ = 1.546 Å for phase identification. XRD patterns were obtained at room temperature in the range 2θ = 10–70° with steps of 0.02°, lasting 30 s for each step. The $ZnCo_2O_4$ crystallite size was calculated by Scherrer's equation [37] using the plane (311) at 2θ = 36.8°:

$$\text{Cristallite size} = \frac{0.89\lambda}{\beta \cos\theta} \frac{180^\circ}{\pi} \quad (1)$$

where λ is the X-ray wavelength and β is the full width at half maximum (FWHM). Raman spectroscopy characterization was performed using a Thermo Scientific DXR confocal Raman microscope with a 633 nm excitation source. The Raman spectra were measured from 150 to 800 cm^{-1} at room temperature, using an exposure time of 60 s and a Laser power of 5 mW. TEM, high-resolution transmission electron microscopy (HRTEM), energy-dispersive X-ray (EDS) and high-angle annular dark-field/scanning transmission electron microscopy (HAADF-STEM) were performed by means of a FEI Tecnai-F30 system operated at 300 kV. The gas sensing measurements were carried out on pellets of $ZnCo_2O_4$ with a thickness of 0.5 mm and a diameter of 12 mm. The pellets were prepared with 0.350 g of $ZnCo_2O_4$ powders employing a manual pressure machine (Simple Ital Equip) at 20 tons for 120 min. A TM20 Leybold detector was used to control the gas concentration and the partial pressure. The sensing response was investigated by measuring the electric resistance using a digital-multimeter (Keithley). The $ZnCo_2O_4$ pellets were exposed to several concentrations (1, 5, 50, 100, 200, and 300 ppm) of CO and C_3H_8. A schematic diagram of the gas sensing measurement system is shown in Figure 1. The gas sensing response, or sensitivity, was defined as $S = R_a/R_g$ for the reducing gas, where R_a and R_g refer to the resistances measured in air and gas, respectively [21,38,39].

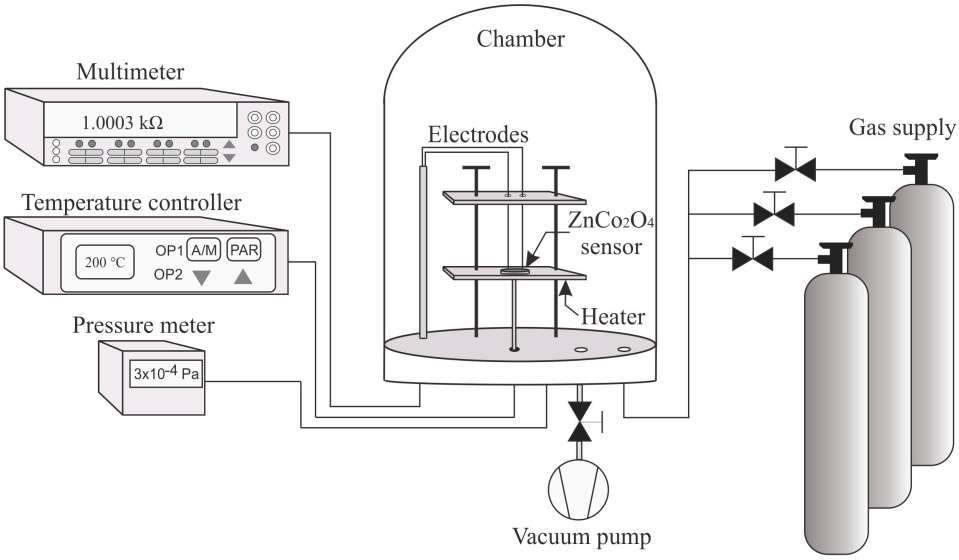

Figure 1. Experimental setup for the gas sensitivity measurements of $ZnCo_2O_4$ nanoparticles.

3. Results and Discussion

SEM images of samples A, B, and C are shown in Figure 2. Sample A exhibited a high concentration of nanoparticles with irregular shape and sizes in the range of 50–110 nm (see Figure 2a,d). Agglomerates of nanoparticles were also observed (Figure 2d). SEM images of sample B revealed a large amount of nanoparticles with diameters in the range from 40–85 nm (see Figure 2b,e). Sample C contained

nanoparticles with diameters ranging from 25–70 nm (Figure 2c,d,f). The particle-size distribution of the three $ZnCo_2O_4$ samples can be seen in Figure 3. From SEM, it is clear that the dodecylamine concentration plays a key role in the morphologies and the particle sizes [40]: an increment of the dodecylamine concentration produced a large amount of nanoparticles and a decreasing particle size, which suggests that the dodecylamine inhibits the growth of the $ZnCo_2O_4$ nanoparticles.

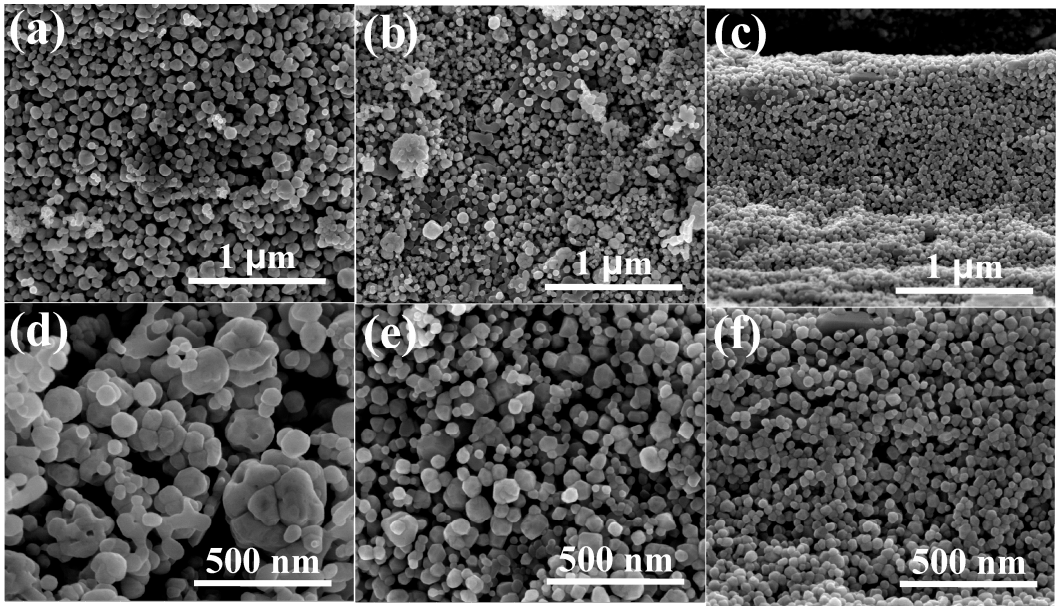

Figure 2. SEM images of $ZnCo_2O_4$ nanoparticles: (**a**,**d**) sample A; (**b**,**e**) sample B; and (**c**,**f**) sample C.

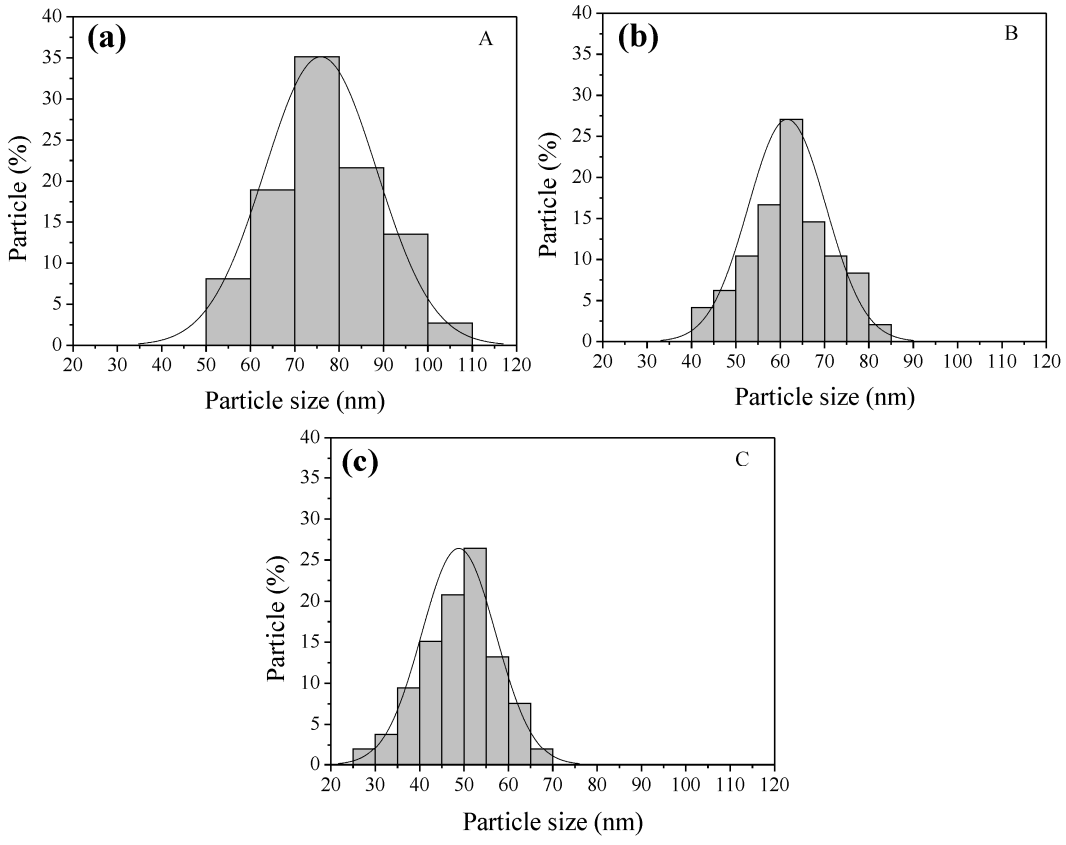

Figure 3. Particle size distribution for the $ZnCo_2O_4$ samples: (**a**) A; (**b**) B; and (**c**) C.

The formation of the $ZnCo_2O_4$ nanoparticles follows the principles of nucleation and growth established by LaMer and Dinegar [41]. In our synthesis, the nucleation process could occur when the zinc nitrate solution was added to the cobalt and dodecylamine solution [30], and the particle growth continued developing by diffusion of the nuclei during agitation of the final solution [42]. As previously discussed, dodecylamine plays an important role in the microstructure of the $ZnCo_2O_4$ particles. In this research, it seems that the ethanol and the dodecylamine are working synergically to reduce cations to metals because ethanol alone is not capable of doing so (i.e., in order to produce ultrafine metal nanoparticles), but just mixed with strong reducing agents such as microwave radiation, other chemical compounds, etc. [43–45]. We have observed that the dodecylamine concentration is the rate-determining factor; therefore, we propose the following reaction mechanism.

Dodecylamine is a primary amine with properties of a weak base because of the nitrogen's unshared electron pair. This kind of amine has nucleophilic behavior and can be used as reducing and surfactant agents. The reaction of dodecylamine with Co^{2+} cations could occur in two ways: (i) the attraction of the unshared electron pair to the nucleus of the cations in a nucleophilic reaction; (ii) the formation of an electrostatic bond between the nitrogen of the dodecylamine and the electrons of the outer shell of Co^{2+}, because of the strong electronegativity of the nitrogen (= 3.04). The result of these interactions is the formation of the dodecylamine-Co^{2+} complex [46]:

$$Co^{2+} + NH_2-(CH_2)_{11}NH_3 \rightarrow Co^{2+} \bullet\bullet\bullet NH_2-(CH_2)_{11}NH_3 \quad (2)$$

In this reaction, dodecylamine is working as the surfactant; therefore, nitrogen's electrons could participate as reducing agents, reducing the cationic Co^{2+} to metallic nanoparticles of Co^0.

$$Co^{2+} + 2e^- \rightarrow Co^0 \quad (3)$$

For 5.4 mmol of dodecylamine, the molar ratio of dodecylamine: Co^{2+} was around 1:2, which suggests that half of the Co^{2+} cations are not participating in the formation of complexes and should be reduced in some way by the solvent. When the dodecylamine-ethanol-Co^{2+} solution is mixed with the ethanol-Zn^{2+} solution, and once the Co^{2+} and Zn^{2+} have been reduced, Zn could attract two atoms of Co to form $ZnCo_2$, as Zn is slightly more electronegative than Co (1.90 vs. 1.65, respectively). Since 5.4 mmol of dodecylamine are not enough to complex all of the Co^{2+} cations, there are several available cations to be reduced by the solvent, and as a result the $ZnCo_2$ grains are the larger ones. For 10.8 mmol of dodecylamine, most of the Co^{2+} should be forming a complex, and the growing of $ZnCo_2$ grains is restricted through the slow release-reduction process of Co^{2+}. For 16.2 mmol of dodecylamine, the Co^{2+} cations could be completely complexed; therefore, the excess of dodecylamine should form complexes even with Zn^{2+}, restricting even more the growing of $ZnCo_2$ grains. Summarizing, the role of dodecylamine is as a surfactant and as a reducing agent; however, it seems that the function of surfactant, through electrostatic interactions, is the dominant one, reducing the particle size and modifying the particles' microstructure as the dodecylamine concentration increases. With heat treatment, the dodecylamine was finally removed from the $ZnCo_2O_4$.

Figure 4 depicts the XRD patterns of the samples. In them, the typical peaks corresponding to the cubic $ZnCo_2O_4$ spinel-structure were identified. The well-defined narrow peaks are an indication of the good crystallinity of the $ZnCo_2O_4$ samples. Table 1 shows the crystallite size of every sample. From these results, an increase in crystallite size was produced when the dodecylamine concentration was increased. A slight increase in the FWHM was also observed, indicating a particle size reduction as was confirmed by SEM.

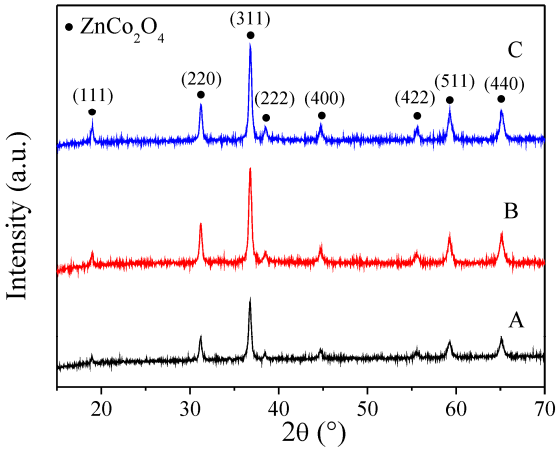

Figure 4. XRD patterns of $ZnCo_2O_4$ samples synthesized with (**A**) 5.4; (**B**) 10.8; and (**C**) 16.2 mmol of dodecylamine. The peak signals for the $ZnCo_2O_4$ structure (JCPDF 23-1390) are labeled with black-filled circles.

Table 1. Crystallite size of the $ZnCo_2O_4$ samples.

Samples	FWHM	Crystallite Size (nm)
A	0.338	24.75
B	0.351	23.84
C	0.421	19.92

The formation of the oxide $ZnCo_2O_4$ was also confirmed by Raman characterization. According to the group theory for oxides with a spinel structure, five active Raman bands were expected: $A_{1g} + E_g + 3F_{2g}$ [47]. Figure 5 shows the Raman spectrum indicating the main vibrational bands produced by the $ZnCo_2O_4$ spinel crystal structure. The bands labeled by v_1, v_3, v_4, v_5, and v_6 correspond to 182, 475, 516, 613, and 693 cm^{-1}, respectively. These bands are assigned to the F_{2g}, E_g, F_{2g}, F_{2g}, and A_{1g} symmetry species. These results are consistent with those reported for $ZnCo_2O_4$ spinel structures [48]. Interestingly, the band located at 204 cm^{-1} (v_2) is a vibrational mode that could be attributed to a Co_3O_4 spinel structure [49]. The formation of Co_3O_4 is likely due to the cation disorder (substitution of Zn^{2+} by Co^{2+}) in the spinel structure of the zinc cobaltite. Notice that the Co_3O_4 possesses a spinel structure similar to that of $ZnCo_2O_4$. Therefore, the XRD patterns between Co_3O_4 and $ZnCo_2O_4$ are almost indistinguishable.

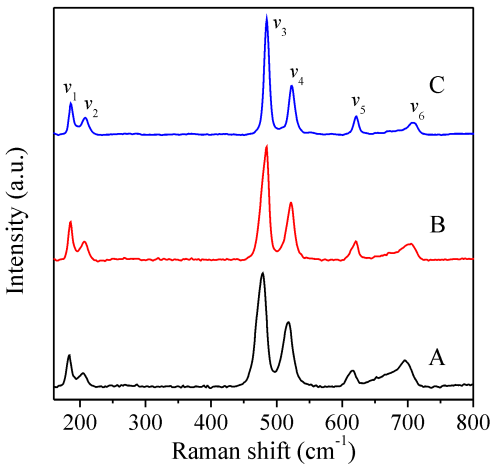

Figure 5. Raman spectra of the samples A, B, and C.

Figure 6 shows TEM images of the samples. The presence of faceted nanoparticles with a pockmarked structure was clearly identified (Figure 6a,c,e). The estimated average particle size was approximately 75, 61, and 49 nm for samples A, B, and C, respectively; these measurements are consistent with the SEM analysis. The standard deviation was ±12.64, ±8.78, and ±8.36 nm, respectively. Figure 6b,d,f shows HRTEM images of the selected area marked with a black rectangle. These images confirmed the presence of faceted $ZnCo_2O_4$ nanoparticles as was done by the XRD patterns and the Raman characterization. Fringe spacings of 0.467 and 0.286 nm are clearly observed, which are attributed to the planes (111) and (220) of the $ZnCo_2O_4$ spinel structure, respectively.

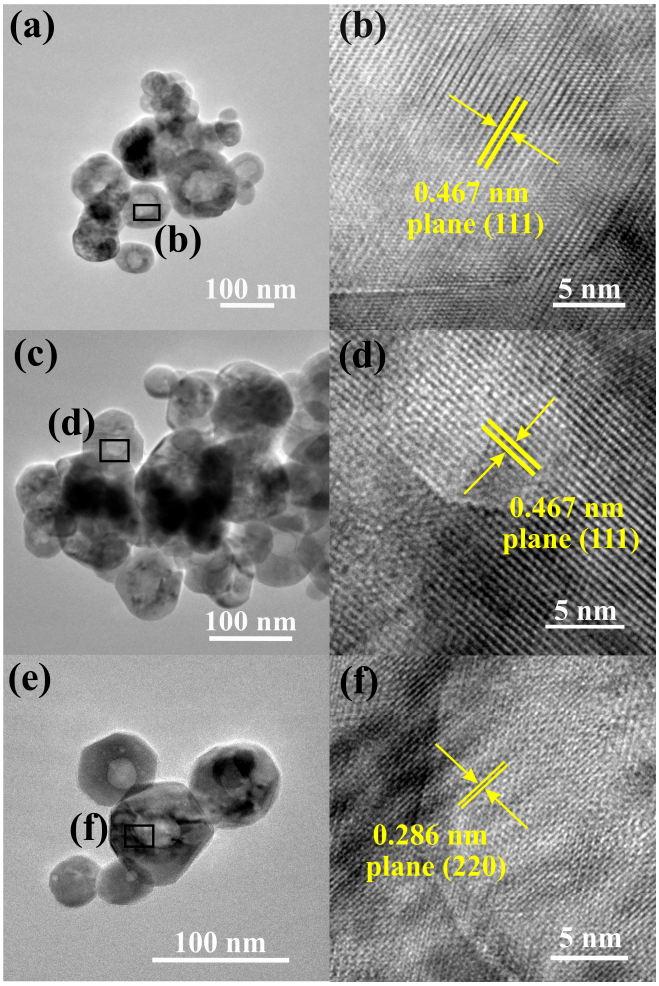

Figure 6. TEM and HRTEM images of the samples A (**a**,**b**); B (**c**,**d**); and C (**e**,**f**).

To investigate the nanoparticle composition, an EDS line scan was performed on sample A (see Figure 7). Figure 7a shows a HAADF-STEM image of the $ZnCo_2O_4$ nanoparticles. The image confirms the presence of faceted nanoparticles with a pockmarked structure, which is consistent with the TEM images. In the EDS line scan, zinc, cobalt, and oxygen are observed across the linear mapping, confirming the presence of the expected elements, as seen in Figure 7b. In the central region p_2, a decrease of the element composition is observed in comparison to point p_1, which can be due to the irregular surface of the nanoparticle (pockmarked zone). Similar EDS elemental line scan spectra were obtained for samples B and C. Figure 7c shows an EDS microanalysis on p_2, where the individual elements Zn, Co, and O can easily be seen. The atomic ratio of Zn:Co is approximately 1:1.96, which is consistent with the composition of $ZnCo_2O_4$. This EDS spectrum is in agreement with the literature [3,5].

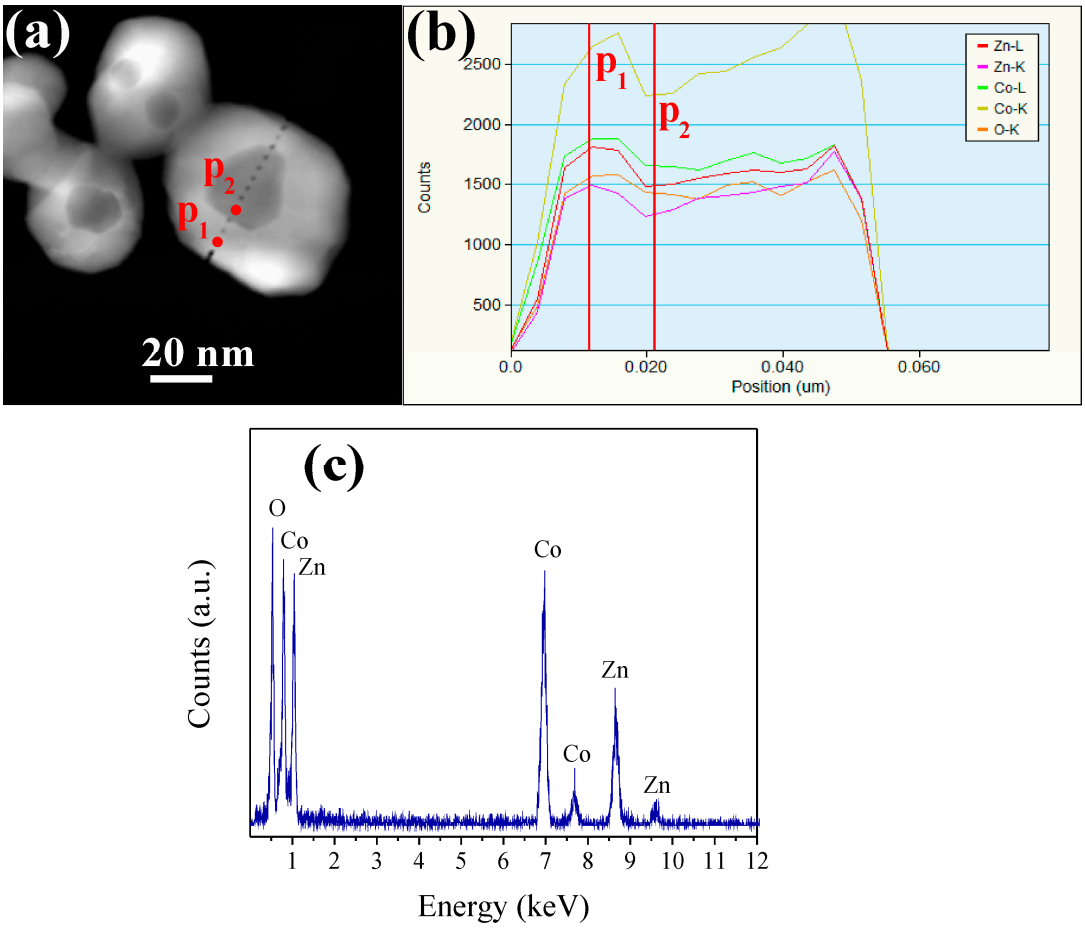

Figure 7. (**a**) HAADF-STEM image; (**b**) elemental line scan; and (**c**) EDS microanalysis of sample A.

To investigate the sensing properties of the $ZnCo_2O_4$ oxide, pellets of the material were made and tested in CO and C_3H_8 atmospheres. Figure 8 shows the oxide's response vs. CO concentration of sensors made from samples A, B, and C. As shown in Figure 8a,c, no response variation was measured for A and C at 100 °C. On the contrary, the sensor made from B exhibited response values of 1, 1.03, 1.21, 1.48, 2.50, and 5.68 for CO concentrations of 1, 5, 50, 100, 200, and 300 ppm, respectively (Figure 8b). At 200 and 300 °C, the response of the three sensors increased with an increase of the CO concentration. In the whole concentration range (1–300 ppm CO), the sensor made from C exhibited a high response at 200 °C, better than the sensors based on A and B. At this temperature, the response values of the sensor based on C were 2.56, 2.66, 3.18, 1274.29, 2622.22, and 2950 for CO concentrations of 1, 5, 50, 100, 200, and 300 ppm, respectively. The sensors made from A and B comparatively also showed a good response to 300 ppm of CO (305.07 and 19.37, respectively) at 300 °C. From these results, it is clear that the $ZnCo_2O_4$ sensors are highly sensitive to concentrations of carbon monoxide and working temperatures. As expected, the material's gas response increased due to the raising of the gas concentration and operation temperature. The raise of the response is associated to an increased oxygen desorption at high temperatures. Some authors report that the response of a semiconductor material depends on the adsorption of several oxygen species as a function of temperature [50,51]. The mechanism to explain the interaction between the CO molecules and a semiconductor oxide like the one used in this work is based on the accumulation layer's modulation due to the chemisorption of oxygen [33,52]. Therefore, in the tests at temperatures above 100 °C, the oxygen species O^- and O^{2-} (ionic form) that adsorb chemically on the sensor are more reactive than other oxygen species that adsorb at temperatures below 100 °C (like O_2^-) [29,36,37]. It means that below 100 °C, the thermal energy is not enough to produce the desorption reactions of the oxygen, and therefore, an electrical

response does not occur regardless of the gas concentration. By contrast, above 100 °C (in this case, 200 and 300 °C), the formation of oxygen species occurs causing an increase in the gas-solid interaction in the presence of CO [33,52,53].

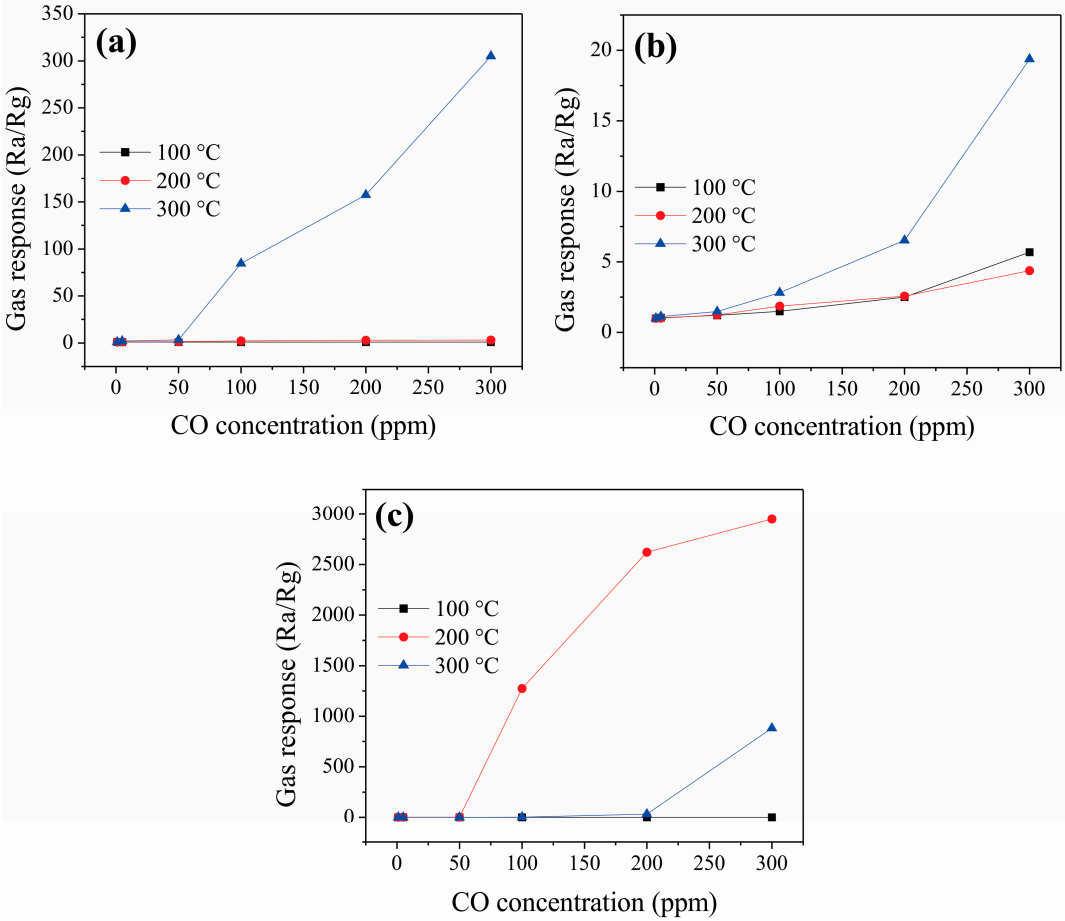

Figure 8. Gas response of $ZnCo_2O_4$ sensors vs. CO concentration at different operating temperatures: (**a**) sample A; (**b**) sample B; and (**c**) sample C.

The response of the $ZnCo_2O_4$ sensors in propane atmospheres at different operating temperatures is shown in Figure 9. Such as in the case of CO, the response rose with the increasing of temperature and propane concentration. However, at temperatures below 100 °C, no changes were observed in the response. At 100 °C, a sensing response value of ~1 was calculated for the sensors A and B in the range of 1–300 ppm of C_3H_8 (Figure 9a,c). At the same temperature, the sensor B registered values of 1, 1.03, 1.13, 1.49, 1.76, and 2.62 for C_3H_8 concentrations of 1, 5, 50, 100, 200, and 300 ppm, respectively (as seen in Figure 9b). Again, the sensor based on sample C also exhibited a higher response than those of A and B at a working temperature of 200 °C. The response values for this sensor C were 1, 1.03, 1.18, 1.56, 1.94, and 8.99 at C_3H_8 concentrations of 1, 5, 50, 100, 200, and 300 ppm, respectively. The sensors based on A and B also exhibited good response to 300 ppm of C_3H_8: 5.89 at 200 °C, and 8 at 300 °C, respectively. Additionally, the three $ZnCo_2O_4$ sensors showed a decrease in gas response when the test gases were removed from the vacuum chamber.

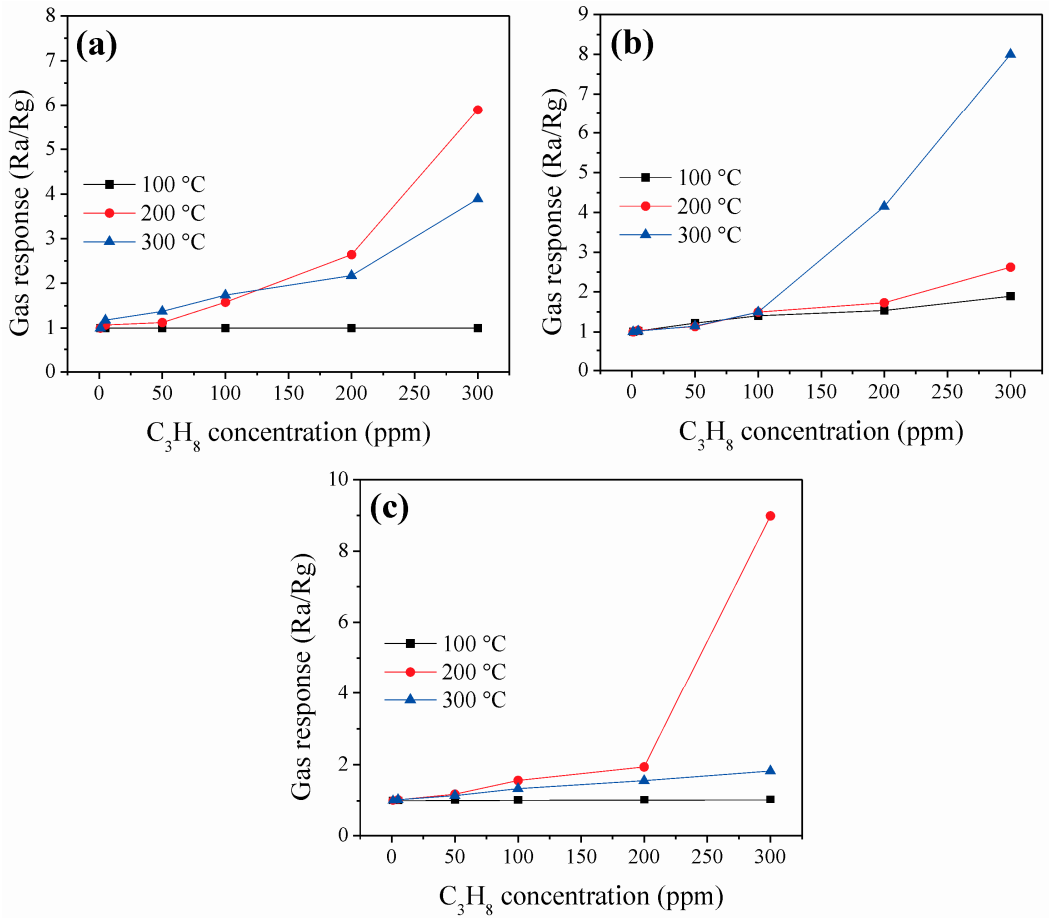

Figure 9. Response of the $ZnCo_2O_4$ sensors as a function of C_3H_8 concentration at different working temperatures: (**a**) sample A; (**b**) sample B; and (**c**) sample C.

As discussed above, the gas detection ability of a material such as the one used in this work depends on the microstructure obtained during the synthesis process [28,29,33,36]. If the particle size is nanometric, the response of the material is substantially improved [54]. It has been established that by reducing the particle size of the materials, their performance (i.e., their sensitivity) to detect different concentrations of gases is boosted [36,55–57], like in our case. Again, the most accepted mechanism to explain the response of the $ZnCo_2O_4$ is based on changes in the electrical resistance (or conductance) due to the adsorption and desorption of oxygen species on the surface [29,54,58–60]. Depending on the semiconductor type, the concentration of surface charge carriers can increase or decrease [59,61]. This is because during the chemical adsorption of oxygen molecules, a hole accumulation layer (space charge layer) is generated [52], provoking a chemical reaction between the gas and the surface of the $ZnCo_2O_4$ and resulting in changes in the electrical resistance of the material (i.e., a high sensitivity is recorded) [38,57]. Additionally, the $ZnCo_2O_4$ response is strongly related to the crystallite size (D), which is less than the thickness of the space charge layer, L_s, defined as [29,54,55,59]:

$$L_s = L_D \sqrt{\frac{eV_s^2}{kT}} \tag{4}$$

where L_D is the Debye length, e is the electron charge, V_s is the surface potential, k is the Boltzmann constant, and T is the absolute temperature. Generally speaking, L_s has a value between 1 and 100 nm [56]. Therefore, the conductivity mechanism is associated with the crystallite size and the space charge layer [29,54,56,62]: if $D >> 2L_s$, the conductivity is limited by the Schottky barrier at the particle

border; thus, gas detection does not depend on the size of the particle; if $D = 2L_s$, the conductivity and the gas sensing depend on the growing of necks formed by crystallites; and when $D < 2L_s$, the conductivity depends on the size of the crystallites. In our case, the latter condition occurs while detecting the gases, since the average particle size is less than 100 nm; that is the reason why the conduction of the charge carriers (holes) takes place on the nanoparticles' surface [56,63].

Comparing the efficiency of our $ZnCo_2O_4$ nanoparticles (a maximum sensitivity of ~2950 and ~8.99 in 300 ppm of CO and C_3H_8, respectively, at 200 °C both) with similar semiconductor oxides, we found in our case greater sensitivity, stability, and efficiency to detect CO and C_3H_8 at different temperatures. For example, references [51,64] reported that $LaCoO_3$ has a maximum sensitivity in the range of 10 to 15 and approximately 42 for CO and C_3H_8 concentrations of 200 and 300 ppm, respectively, at 350 °C. For the SnO_2 oxide, they reported a sensitivity of ~0.6 and ~0.7 at 300 °C in a concentration of 500 ppm for both gases. Reference [33] reported that the oxide $ZnSb_2O_6$ showed a maximum sensitivity of ~6.66 and ~1.2 at 250 °C for CO and C_3H_8, respectively. Reference [54] reported that the oxide $CoSb_2O_6$ had a sensitivity of ~4.8 at 350 °C in 300 ppm of C_3H_8. In the case of zinc-cobaltites, our $ZnCo_2O_4$ shows a superior gas sensing response than those synthesized by Vijayanand et al. [15], which had a sensitivity of ~1 in 50 ppm of CO at 350 °C; those by Zhou et al. (using sensors based on $ZnO/ZnCo_2O_4$ composites) [21], who obtained a response of ~1.1 in 100 ppm of CO at 275 °C; those by Liu et al. (using a sensor based on porous $ZnCo_2O_4$ nano/microspheres) [20], who obtained a response of ~2 in 100 ppm of CO at 175 °C; and recently, those by Long et al. [22], who reported a sensitivity of ~29 and ~13 at 300 °C in 10 ppm of CO and in 5000 ppm of C_3H_8, respectively.

4. Conclusions

In this work, we successfully synthesized $ZnCo_2O_4$ faceted nanoparticles with a size between 49 and 75 nm by means of a simple, economical, and efficient route: the microwave-assisted colloidal method using dodecylamine as a surfactant agent and a calcination temperature of 500 °C. Sensors prepared with these nanoparticles exhibited an excellent response (~2950 with sample C) at a relatively low operating temperature (200 °C) for the detection of CO, and they were capable of detecting up to 300 ppm of C_3H_8 at 200 °C, which is comparatively (with similar oxides) a very good performance. Hence, $ZnCo_2O_4$ is a promising material for applications as a gas sensor, especially in the detection of CO and C_3H_8.

Acknowledgments: The authors are grateful to G. J. Labrada-Delgado, B. A. Rivera-Escoto, K. Gomez, Miguel Ángel Luna-Arias, and Sergio Oliva for their technical assistance. CONACYT-Mexico grants: the National Laboratory for Nanoscience and Nanotechnology Research (LINAN). J. P. Morán acknowledges financial support from F-PROMEP-39/Rev-04 SEP-23-005 and PROFOCIE 2016.

Author Contributions: J.P.M.-L. designed the research, performed the synthesis of the material and the structural characterization, and wrote the manuscript. F.L.-U. carried out the morphological characterizations and contributed to the preparation of the manuscript. E.M.-S. gave many helpful suggestions about characterizations. O.B.-A., M.S.-T. and A.C.-A. provided a contribution on data interpretation. H.G.-B. and M.L.O.-A. supported with sensing measurements. A.G.-B. and V.M.R.-B. performed the Raman experiments.

Conflicts of Interest: The authors declare no conflict of interest.

References

1. Sharma, Y.; Sharma, N.; Subba-Rao, G.V.; Chowdari, B.V.R. Nanophase $ZnCo_2O_4$ as a high performance anode material for Li-ion batteries. *Adv. Funct. Mater.* **2007**, *17*, 2855–2861. [CrossRef]
2. Du, N.; Xu, Y.; Zhang, H.; Yu, J.; Zhai, C.; Yang, D. Porous $ZnCo_2O_4$ nanowires synthesis via sacrificial templates: High-performance anode materials of Li-ion batteries. *Inorg. Chem.* **2011**, *50*, 3320–3324. [CrossRef] [PubMed]
3. Huang, L.; Waller, G.H.; Ding, Y.; Chen, D.; Ding, D.; Xi, P.; Wang, Z.L.; Liu, M. Controllable interior structure of $ZnCo_2O_4$ microspheres for high-performance lithium-ion batteries. *Nano Energy* **2015**, *11*, 64–70. [CrossRef]

4. Bai, J.; Li, X.; Liu, G.; Qian, Y.; Xiong, S. Unusual formation of $ZnCo_2O_4$ 3D hierarchical twin microspheres as a high-rate and ultralong-life lithium-ion battery anode material. *Adv. Funct. Mater.* **2014**, *24*, 3012–3020. [CrossRef]
5. Liu, B.; Zhang, J.; Wang, X.; Chen, G.; Chen, D.; Zhou, C.; Shen, G. Hierarchical three-dimensional $ZnCo_2O_4$ nanowire arrays/carbon cloth anodes for a novel class of high-performance flexible lithium-ion batteries. *Nano Lett.* **2012**, *12*, 3005–3011. [CrossRef] [PubMed]
6. Kim, T.W.; Woo, M.A.; Regis, M.; Choi, K.-S. Electrochemical synthesis of spinel type $ZnCo_2O_4$ electrodes for use as oxygen evolution reaction catalysts. *J. Phys. Chem. Lett.* **2014**, *5*, 2370–2374. [CrossRef] [PubMed]
7. Wang, S.; Ding, Z.; Wang, X. A stable $ZnCo_2O_4$ cocatalyst for photocatalytic CO_2 reduction. *Chem. Commun.* **2015**, *51*, 1517–1519. [CrossRef] [PubMed]
8. Wang, H.; Song, X.H.; Wang, H.Y.; Bi, K.; Liang, C.; Lin, S.; Zhang, R.; Du, Y.X.; Liu, J.; Fan, D.Y.; et al. Synthesis of hollow porous $ZnCo_2O_4$ microspheres as high-performance oxygen reduction reaction electrocatalyst. *Int. J. Hydrog. Energy* **2016**, *41*, 13024–13031. [CrossRef]
9. Zhang, J.; Zhang, D.; Yang, Y.; Ma, J.; Cui, S.; Li, Y.; Yuan, B. Facile synthesis of $ZnCo_2O_4$ mesoporous structures with enhanced electrocatalytic oxygen evolution reaction properties. *RSC Adv.* **2016**, *6*, 92699–92704. [CrossRef]
10. Zhou, G.; Zhu, J.; Chen, Y.; Mei, L.; Duan, X.; Zhang, G.; Chen, L.; Wang, T.; Lu, B. Simple method for the preparation of highly porous $ZnCo_2O_4$ nanotubes with enhanced electrochemical property for supercapacitor. *Electrochim. Acta* **2014**, *123*, 450–455. [CrossRef]
11. Wu, C.; Cai, J.; Zhang, Q.; Zhou, X.; Zhu, Y.; Li, L.; Shen, P.; Zhang, K. Direct growth of urchin-like $ZnCo_2O_4$ microspheres assembled from nanowires on nickel foam as high-performance electrodes for supercapacitors. *Electrochim. Acta* **2015**, *169*, 202–209. [CrossRef]
12. Fu, W.; Li, X.; Zhao, C.; Liu, Y.; Zhang, P.; Zhou, J.; Pan, X.; Xie, E. Facile hydrothermal synthesis of flower like $ZnCo_2O_4$ microspheres as binder-free electrodes for supercapacitors. *Mater. Lett.* **2015**, *169*, 1–4. [CrossRef]
13. Chang, S.-K.; Zainal, Z.; Tan, K.-B.; Yusof, N.A.; Yusoff, W.M.D.W.; Prabaharan, S.R.S. Recent development in spinel cobaltites for supercapacitor application. *Ceram. Int.* **2015**, *41*, 1–14. [CrossRef]
14. Mariappan, C.R.; Kumara, R.; Vijaya, P. Functional properties of $ZnCo_2O_4$ nano-particles obtained by thermal decomposition of a solution of binary metal nitrates. *RSC Adv.* **2015**, *5*, 26843–26849. [CrossRef]
15. Vijayanand, S.; Joy, P.A.; Potdar, H.S.; Patil, D.; Patil, P. Nanostructured spinel $ZnCo_2O_4$ for the detection of LPG. *Sens. Actuators B Chem.* **2011**, *152*, 121–129. [CrossRef]
16. Gawande, K.B.; Gawande, S.B.; Thakare, S.R.; Mate, V.R.; Kadam, S.R.; Kale, B.B.; Kulkarni, M.V. Effect of zinc: Cobalt composition in $ZnCo_2O_4$ spinels for highly selective liquefied petroleum gas sensing at low and high temperatures. *RSC Adv.* **2015**, *5*, 40429–40436. [CrossRef]
17. Bangale, S.V.; Khetre, S.M.; Patil, D.R.; Bamane, S.R. Simple Synthesis of $ZnCo_2O_4$ nanoparticles as gas-sensing materials. *Sens. Transducers J.* **2011**, *134*, 95–106.
18. Niu, X.; Du, W.; Du, W. Preparation and gas sensing properties of ZnM_2O_4 (M = Fe, Co, Cr). *Sens. Actuators B Chem.* **2004**, *99*, 405–409. [CrossRef]
19. Zhang, G.-Y.; Guo, B.; Chen, J. MCo_2O_4 (M = Ni, Cu, Zn) nanotubes: Template synthesis and application in gas sensors. *Sens. Actuators B Chem.* **2006**, *114*, 402–409. [CrossRef]
20. Liu, T.; Liu, J.; Liu, Q.; Song, D.; Zhang, H.; Zhang, H.; Wang, J. Synthesis, characterization and enhanced gas sensing performance of porous $ZnCo_2O_4$ nano/microspheres. *Nanoscale* **2015**, *7*, 19714–19721. [CrossRef] [PubMed]
21. Zhou, X.; Feng, W.; Wang, C.; Hu, X.; Li, X.; Sun, P.; Shimanoe, K.; Yamazoe, N.; Lu, G. Porous ZnO/$ZnCo_2O_4$ hollow spheres: Synthesis, characterization, and applications in gas sensing. *J. Mater. Chem. A.* **2014**, *2*, 17683–17690. [CrossRef]
22. Long, H.; Harley-Trochimczyk, A.; Cheng, S.; Hu, H.; Chi, W.S.; Rao, A.; Carraro, C.; Shi, T.; Tang, Z.; Maboudian, R. Nanowire-assembled hierarchical $ZnCo_2O_4$ microstructure integrated with a low-power microheater for highly sensitive formaldehyde detection. *ACS Appl. Mater. Interfaces* **2016**, *8*, 31764–31771. [CrossRef] [PubMed]
23. Park, H.J.; Kim, J.; Choi, N.-J.; Song, H.; Lee, D.-S. Nonstoichiometric Co-rich $ZnCo_2O_4$ hollow nanospheres for high performance formaldehyde detection at ppb levels. *ACS Appl. Mater. Interfaces* **2016**, *8*, 3233–3240. [CrossRef] [PubMed]

24. Yamazoe, N. New approaches for improving semiconductor gas sensors. *Sens. Actuators B Chem.* **1991**, *5*, 7–19. [CrossRef]
25. Wei, X.; Chen, D.; Tang, W. Preparation and characterization of the spinel oxide $ZnCo_2O_4$ obtained by sol-gel method. *Mater. Chem. Phys.* **2007**, *103*, 54–58. [CrossRef]
26. Wang, Y.; Wang, M.; Chen, G.; Dong, C.; Wang, Y.; Fan, L.-Z. Surfactant-mediated synthesis of $ZnCo_2O_4$ powders as a high-performance anode material for li-ion batteries. *Ionics* **2015**, *21*, 623–628. [CrossRef]
27. Morán-Lázaro, J.P.; Blanco, O.; Rodríguez-Betancourtt, V.M.; Reyes-Gómez, J.; Michel, C.R. Enhanced CO_2-sensing response of nanostructured cobalt aluminate synthesized using a microwave-assisted colloidal method. *Sens. Actuators B Chem.* **2016**, *226*, 518–524. [CrossRef]
28. Guillen-Bonilla, H.; Reyes-Gomez, J.; Guillen-Bonilla, A.; Pozas-Zepeda, D.; Guillen-Bonilla, J.T.; Gildo-Ortiz, L.; Flores-Martinez, M. Synthesis and characterization of $MgSb_2O_6$ trirutile-type in low presence concentrations of ethylenediamine. *J. Chem. Chem. Eng.* **2013**, *7*, 395–401.
29. Guillén-Bonilla, A.; Rodríguez-Betancourtt, V.-M.; Flores-Martínez, M.; Blanco-Alonso, O.; Reyes-Gómez, J.; Gildo-Ortiz, L.; Guillén-Bonilla, H. Dynamic response of $CoSb_2O_6$ trirutile-type oxides in a CO_2 atmosphere at low-temperatures. *Sensors* **2014**, *14*, 15802–15814. [CrossRef] [PubMed]
30. Blanco, O.; Morán-Lázaro, J.P.; Rodríguez-Betancourtt, V.M.; Reyes-Gómez, J.; Barrera, A. Colloidal synthesis of $CoAl_2O_4$ nanoparticles using dodecylamine and their structural characterization. *Superficies y Vacío* **2016**, *29*, 78–82.
31. Mirzaei, A.; Neri, G. Microwave-assisted synthesis of metal oxide nanostructures for gas sensing application: A review. *Sens. Actuators B Chem.* **2016**, *237*, 749–775. [CrossRef]
32. Hu, S.-Y.; Lee, Y.-C.; Chen, B.-J. Characterization of calcined $CuInS_2$ nanocrystals prepared by microwave-assisted synthesis. *J. Alloys Compd.* **2017**, *690*, 15–20. [CrossRef]
33. Guillen-Bonilla, H.; Rodríguez-Betancourtt, V.M.; Guillén-Bonilla, J.T.; Reyes-Gómez, J.; Gildo-Ortiz, L.; Flores-Martínez, M.; Olvera-Amador, M.L.; Santoyo-Salazar, J. CO and C_3H_8 sensitivity behavior of zinc antimonate prepared by a microwave-assisted solution method. *J. Nanomater.* **2015**, *2015*. [CrossRef]
34. Bing, Y.; Zeng, Y.; Liu, C.; Qiao, L.; Zheng, W. Synthesis of double-shelled SnO_2 nano-polyhedra and their improved gas sensing properties. *Nanoscale* **2015**, *7*, 3276–3284. [CrossRef] [PubMed]
35. Zhang, H.; Song, P.; Han, D.; Yan, H.; Yang, Z.; Wang, Q. Controllable synthesis of novel $ZnSn(OH)_6$ hollow polyhedral structures with superior ethanol gas-sensing performance. *Sens. Actuators B Chem.* **2015**, *209*, 384–390. [CrossRef]
36. Guillén-Bonilla, H.; Flores-Martínez, M.; Rodríguez-Betancourtt, V.M.; Guillén-Bonilla, A.; Reyes-Gómez, J.; Gildo-Ortiz, L.; Olvera-Amador, M.L.; Santoyo-Salazar, J. A novel gas sensor based on $MgSb_2O_6$ nanorods to indicate variations in carbon monoxide and propane concentrations. *Sensors* **2016**, *16*, 177. [CrossRef] [PubMed]
37. Ji, Y.; Zhao, Z.; Duan, A.; Jiang, G.; Liu, J. Comparative study on the formation and reduction of bulk and Al_2O_3-supported cobalt oxides by H_2-TPR technique. *J. Phys. Chem. C* **2009**, *113*, 7186–7199. [CrossRef]
38. Wang, C.; Yin, L.; Zhang, L.; Xiang, D.; Gao, R. Metal oxide gas sensors: Sensitivity and influencing factors. *Sensors* **2010**, *10*, 2088–2106. [CrossRef] [PubMed]
39. Qu, F.; Jiang, H.; Yang, M. Designed formation through a metal organic framework route of $ZnO/ZnCo_2O_4$ hollow core–shell nanocages with enhanced gas sensing properties. *Nanoscale* **2016**, *8*, 16349–16356. [CrossRef] [PubMed]
40. Bekhti, W.; Ghamnia, M.; Guerbous, L. Effect of some amines, dodecylamine (DDA) and hexadecyldimethylamine (DMHA), on the formation of ZnO nanorods synthesized by hydrothermal route. *Philos. Mag.* **2014**, *94*, 2886–2899. [CrossRef]
41. LaMer, V.K.; Dinegar, R.H. Theory, production and mechanism of formation of monodispersed hydrosols. *J. Am. Chem. Soc.* **1950**, *72*, 4847–4854. [CrossRef]
42. Vekilov, P.G. What determines the rate of growth of crystals from solution? *Cryst. Growth Des.* **2007**, *7*, 2796–2810. [CrossRef]
43. Itakura, T.; Toringo, K.; Esumi, K. Preparation and characterization of ultrafine metal particles in ethanol by UV irradiation using a photoinitiator. *Langmuir* **1995**, *11*, 4129–4134. [CrossRef]
44. Pal, A.; Shan, S.; Devi, S. Microwave-assisted synthesis of silver nanoparticles using ethanol as a reducing agent. *Mater. Chem. Phys.* **2009**, *114*, 530–532. [CrossRef]

45. Ayyappan, S.; Gopalan, R.S.; Subbanna, G.N.; Rao, C.N.R. Nanoparticles of Ag, Au, Pd, and Cu produced by alcohol reduction of the salts. *J. Mater. Res.* **1997**, *12*, 398–401. [CrossRef]
46. Yang, J.; Sargent, E.; Kelley, S.; Ying, J.Y. A general phase-transfer protocol for metal ions and its application in nanocrystal synthesis. *Nat. Mater.* **2009**, *8*, 683–689. [CrossRef] [PubMed]
47. Julien, C.M.; Gendron, F.; Amdouni, A.; Massot, M. Lattice vibrations of materials for lithium rechargeable batteries. VI: Ordered Spinels. *Mater. Sci. Eng. B.* **2006**, *130*, 41–48. [CrossRef]
48. Samanta, K.; Bhattacharya, P.; Katiyar, R.S. Raman scattering studies in dilute magnetic semiconductor $Zn_{1-x}Co_xO$. *Phys. Rev. B* **2006**, *73*, 245213. [CrossRef]
49. Shirai, H.; Morioka, Y.; Nakagawa, I. Infrared and Raman spectra and lattice vibrations of some oxide spinels. *J. Phys. Soc. Jpn.* **1982**, *51*, 592–597. [CrossRef]
50. Chang, S.C. Oxygen chemisorption on tin oxide: Correlation between electrical conductivity and EPR measurements. *J. Vac. Sci. Technol.* **1979**, *17*, 366–369. [CrossRef]
51. Gildo-Ortiz, L.; Guillén-Bonilla, H.; Santoyo-Salazar, J.; Olvera, M.L.; Karthik, T.V.K.; Campos-González, E.; Reyes-Gómez, J. Low-temperature synthesis and gas sensitivity of perovskite-type $LaCoO_3$ nanoparticles. *J. Nanomater.* **2014**, *2014*, 61. [CrossRef]
52. Kim, H.-J.; Lee, J.-H. Highly sensitive and selective gas sensors using p-type oxide semiconductors: Overview. *Sens. Actuators B Chem.* **2014**, *192*, 607–627. [CrossRef]
53. Hübner, M.; Simion, C.E.; Haensch, A.; Barsan, N.; Weimar, U. CO sensing mechanism with WO_3 based gas sensors. *Sens. Actuators B Chem.* **2010**, *151*, 103–106. [CrossRef]
54. Guillén-Bonilla, H.; Gildo-Ortiz, L.; Olvera, M.L.; Santoyo-Salazar, J.; Rodríguez-Betancourtt, V.-M.; Guillen-Bonilla, A.; Reyes-Gómez, J. Sensitivity of mesoporous $CoSb_2O_6$ nanoparticles to gaseous CO and C_3H_8 at low temperatures. *J. Nanomater.* **2015**, *2015*. [CrossRef]
55. Korotcenkov, G. Metal oxides for solid-state gas sensors: What determines our choice? *Mater. Sci. Eng. B Chem.* **2007**, *139*, 1–23. [CrossRef]
56. Bochenkov, V.E.; Sergeev, G.B. Preparation and chemiresistive properties of nanostructured materials. *Adv. Colloid Interface Sci.* **2005**, *116*, 245–254. [CrossRef] [PubMed]
57. Yamazoe, N. Toward innovations of gas sensor technology. *Sens. Actuators B Chem.* **2005**, *108*, 2–14. [CrossRef]
58. Karthik, T.V.K.; Olvera-Amador, M.L.; Maldonado, A.; Gómez-Pozos, H. CO Gas sensing properties of pure and Cu-incorporated SnO_2 nanoparticles: A study of Cu-induced modifications. *Sensors* **2016**, *16*, 1283. [CrossRef] [PubMed]
59. Jin, Z.; Zhou, H.J.; Jin, Z.L.; Savinell, R.F.; Liu, C.C. Application of nano-crystalline porous tin oxide thin film for CO sensing. *Sens. Actuators B Chem.* **1998**, *52*, 188–194. [CrossRef]
60. Neri, G. First fifty years of chemoresistive gas sensors. *Chemosensors* **2015**, *3*, 1–20. [CrossRef]
61. Moseley, P.T. Materials selection for semiconductor gas sensors. *Sens. Actuators B Chem.* **1992**, *6*, 149–156. [CrossRef]
62. Xu, C.; Tamaki, J.; Miura, N.; Yamazoe, N. Grain size effects on gas sensitivity of porous SnO_2-based elements. *Sens. Actuators B Chem.* **1991**, *3*, 147–155. [CrossRef]
63. Tan, O.K.; Cao, W.; Hu, Y.; Zhu, W. Nano-structured oxide semiconductor materials for gas-sensing applications. *Ceram. Int.* **2004**, *30*, 1127–1133. [CrossRef]
64. Gómez-Pozos, H.; González-Vidal, J.L.; Alberto-Torres, G.; Olvera, M.L.; Castañeda, L. Physical characterization and effect of effective surface area on the sensing properties of tin dioxide thin solid films in a propane atmosphere. *Sensors* **2014**, *14*, 403–415. [CrossRef]